Propane gas-sensing properties of pure and Pd-doped tin oxide nanostructures

T. V. K. Karthik[1], M. de la L. Olvera-Amador[2], Arturo Maldonado[2], Angélica G. Hernandez[1], and Heberto Gómez-Pozos[3,*] (iD)

[1] *Escuela Superior de Tepeji del Río, Ingeniería Industrial, Universidad Autónoma del Estado de Hidalgo, Avenida del Maestro No. 41 Colonia Noxtongo, Segunda Sección, 42855 Tepeji del Río, Hidalgo, Mexico*

[2] *SEES, Departamento de Ingeniería Eléctrica, Centro de Investigación y de Estudios Avanzados del Instituto Politécnico Nacional, CINVESTAV-IPN, 07000 Mexico City, Mexico*

[3] *Área Académica de Computación y Electrónica, Universidad Autónoma del Estado de Hidalgo, 56092 Pachuca, Hidalgo, Mexico*

ABSTRACT

Pure and palladium-doped tin oxide nanopowders were synthesized by wet chemical synthesis with Tin (IV) chloride pentahydrate and palladium (II) chloride as a precursor and dopant source, respectively. Effect of palladium (Pd) concentration on the structural, morphological, and propane gas-sensing properties were studied in detail. X-ray diffraction analysis confirms the tetragonal rutile phase structure with (110) as the preferential orientation of SnO_2. Also, the presence of Pd and PdO phases was observed confirming the formation of dopant clusters on the surface. The dopant incorporation into the SnO_2 lattice was also observed by Raman analysis with a right shift in the vibrational mode. Scanning Electron Microscopy (SEM) studies show the formation of both large and small grains with irregular shapes and nanometric crystallites. High-resolution Transmission electron microscopy (HRTEM) confirms the tetragonal shape of the particles and the undulations observed due to dopant incorporation and the formation of surface dopant clusters. Gas-sensing responses of all SnO_2 powder were obtained for propane gas, at different gas concentrations and operating temperatures. The highest sensing response was obtained for SnO_2 powder deposited at 4 wt%. By utilizing a simple chemical synthesis and pellet manufacturing, a high surface area-doped nanostructures were obtained, which show the highest propane-sensing response. Finally, in this work, a complete and systematic structural and morphological analysis of all samples were performed and the effect of Pd doping wt% on the propane gas sensing of SnO_2 structures was clearly explained utilizing a schematic sensing mechanism.

Address correspondence to E-mail: gpozos@uaeh.edu.mx

✌ Springer

1 Introduction

Tin oxide (SnO_2) is a metal oxide semiconductor with high durability [1], chemical stability [2], direct wide bandgap (~ 3.3 eV) [3], and optical transmittance (80–90%). This semiconductor has a wide variety of applications in several areas such as electronic [4], optical [5], and biological [6] fields. In addition, tin oxide is one of the first materials tested for gas sensing and is mostly utilized in available commercial gas sensor devices. Furthermore, SnO_2 is widely used as gas sensor due to its low cost, high abundance on earth, and ecofriendly, easy synthesis, which is very suitable to be employed in industry and homes.

Increasing in the human activity such as transport, industrial production, and deforestations, among others [7], has originated an increment of the pollution in the environment and, therefore, putting in risk the normal development of any type of life. Moreover, monitoring of air quality is a powerful tool since the identification of pollutants in the air as well as their concentration allows to take actions for its reductions and degradation. Gas sensing provides a reliable assessment for evaluating the quality and performance of clean energies, renewable technologies, and ecofriendly devices for safe technological applications. Most of the pollutants that are released into the atmosphere come from products derived from hydrocarbons, such as carbon dioxide (CO_2) [8], sulfur dioxide (SO_2) [9], nitrogen oxides (NO) [10], and propane (C_3H_8) [11] among others. Propane, widely used in home stoves and at several industrial activities and it is a corrosive, flammable, odor less, and color less gas. It has been monitored by semiconductor oxides such as TiO_2 [12], $MgSb_2O_6$ [13], CdS, [14], ZnO [15], and SnO_2 [16].

Gas sensors generally work with principle of change in surface electrical resistance or electrical conductance due to the interchange of charge carries from test gas molecules onto the semiconductor surface. The overall quality of the gas sensors depends on different factors, from which two play a significant role: the surface morphology and the number of active sites on the surface of the gas sensor. In the first case, it has been found that the surface to-volume ratio increases in grains with sizes of few tens of nanometers, improving the performance of a semiconductor as a gas sensor [17]. On the other hand, the number of electrically active sites on the surface can be increased by the incorporation of dopant atoms which takes substitutional/interstitial positions on the surface and acts as a catalytic agent resulting in the improvement of sensing response [18]. Enhancement of gas-sensing performance has been reported in the SnO_2 doped with catalytic metals such as In [19], Ga [20], Al [21], and Pd [22]. Theoretical and experimental studies have shown that Pd occupies substitutional sites of Sn and causes very slight distortion in the crystal lattice due to its comparable ionic radii with Sn (Ionic radii of Sn and Pd are 0.71 and 0.64 Å, respectively) [23]. Chemical methods like precipitation, sol gel, among others [24, 25] have been used to obtain SnO_2 nanostructures (either films or powders) with higher gas-sensing responses. Among them, dip coating [26], ultrasonic spray pyrolysis [27], and homogeneous precipitation [28] are cost-effective non-vacuum method, and relatively easy to perform although it is worthy to note that complex physics-chemical reactions take place during synthesis.SnO_2 with good physical characteristics which depend to their nature of synthesis has been reported [29–32]. In comparison with thin films, powders or pellets possess more surface area and high porosity making the surface to interact with more amount of target gas molecules.

In general, a large amount of works has been reported in utilizing Pd-doped SnO_2 nanostructures for detecting acetone, hydrogen, carbon monoxide, or ethanol vapors. Very few works have been reported in the last 2 decades [33–35] for detecting liquid petroleum gas (LPG) or propane. For example, Srivastava et al. [33] reported the preparation of Pd-doped SnO_2 thick films by screen printing and its LPG sensing. In this work, commercially available tin oxide pasted was utilized and the highest sensitivity achieved was around 70% for 1 wt% Pd-doped tin oxide. However, authors mention clearly in the work that LPG contains both butane and propane components, and the selective detection of the propane was not reported. Additionally, morphological and structural properties of the obtained thick films were also not discussed in the above-mentioned work. Also, Lohia reported [34] a theoretical implementation of artificial neural network for detecting LPG gas by Pd-doped SnO_2 sensors and achieved 72% of sensing at 350 °C. However, authors in this work did not discuss the effect of Pd doping on the structural and morphological properties of the sensors. In addition, Phani reported the XPS studies of Pd-doped

SnO_2 petroleum sensor in which author achieved a sensitivity around 97% for 1.5 wt% Pd-doped SnO_2 at 350 °C, and the sensors were obtained by coprecipitation method. However, this work also did not provide the effect of different physical parameters on the gas-sensing mechanism of LPG. Also, authors mentioned that the test gas contained 80% of butane and only 10% of propane. Based on all these previous reports, it is still pending the fabrication of pure propane gas sensors (not LPG) and discuss their gas-sensing mechanism based on different structural and morphological properties. To the best of our knowledge, the preparation of Pd-doped SnO_2 pellet sensors by wet chemical synthesis, and their utilization for detecting propane gas with all the structural and morphological properties has not been reported yet.

In this work, the preparation of undoped and Pd-doped SnO_2pellets to detect propane gas has been carried out. The pellets were prepared by utilizing SnO_2 powders synthetized with ammonium hydroxide as precipitation agent. Powders were obtained by using the tin (IV) chloride pentahydrate as starting solution and palladium (II) chloride as doping solution. The purpose of this work is to analyze the nanostructured surfaces and the doping concentration pellets on the sensor's performance.

2   Experimental procedure

2.1   Pure and Pd-doped SnO_2 powders preparation

Two separate 0.4 M aqueous solutions of tin chloride (IV) pentahydrate ($SnCl_4 \cdot 5H_2O$, Sigma Aldrich, USA) and ammonia (NH_4OH, Sigma Aldrich, United State) were prepared. The ammonia solution was added drop by drop into the tin chloride solution until the pH reaches 12. The resulted precipitates obtained were dried at 100 °C for 24 h in a drying oven and subsequent calcinating process in air at 800 °C for 120 min.

For the preparation of doped SnO_2 powders, a proportionate amount (0.5, 1, 2, and 4 wt%) of palladium (II) chloride ($PdCl_2$, Sigma Aldrich, USA) was added in the starting solution and the similar procedure as in the case of pure SnO_2 powders is followed. Figure 1 demonstrates the over synthesis procedure.

2.2   Sensor fabrication

Pure and Pd-doped SnO_2 pellets of each sample were obtained by considering 1.0 g of each sample and pressed in a 1.2 mm die (Fig. 2b) with an IMR-pressing machine (Fig. 2a). Pellets were obtained with a force of 16 tons for 90 min, the diameter of the obtained pellet was 12 mm, and the weight of each pellet is between 0.45 and 0.48 g, with the average thickness of 0.5 mm ± 10%. Subsequently, silver contacts were drop casted over each using commercially available silver conductive paint. Finally, before gas-sensing measurements, all the pellets were calcinated at 200 °C for 15 min in order to remove any residues of silver paint. Figure 2c shows the overall flow chart of the material fabrication process.

2.3   Characterization

The structural properties of SnO_2 pellets were investigated by X-ray diffraction with Cu-Kα1 ($\lambda = 1.5418$ Å) radiation, with an angle ranging between 20 and 80°. Scanning Electron Microscopy (SEM) JEOL JSM-5900LV was employed to study the surface morphology of the surface. High-resolution transmission electron microscope (HRTEM JEM-ARF 200F) analysis was performed to confirm the crystal size, dopant location, and lattice spacing.

All the vibrational modes of the pure and doped SnO_2 samples were performed by Raman analysis with 532 nm laser beams and detecting scattering signals by a thermoelectrically cooled charge coupled detector. In order to investigate the sensor response, surface electrical resistance measurements in air and in different concentrations of propane gas were obtained and according to Eq. (1):

$$Sensor \; response = \frac{G_G - G_O}{G_O},$$ (1)

where G_G is the surface electrical conductance in the presence of different concentrations of C_3H_8, 1, 5, 50, 100, 200, and 300 ppm, and G_O is the surface electrical conductance in vacuum (0.61×10^{-3} atm minimum base pressure). The surface electrical conductance was obtained from the inverse of surface electrical resistance, a Keithley 2001 digital multimeter with 1 GΩ range, 100 Ω resolution, and 4.4 nA current source were used. Each sample was placed into a chamber with a chamber volume of 12,800 cm^3 and propane gas (C_3H_8, Praxair, 1000 ppm, balance

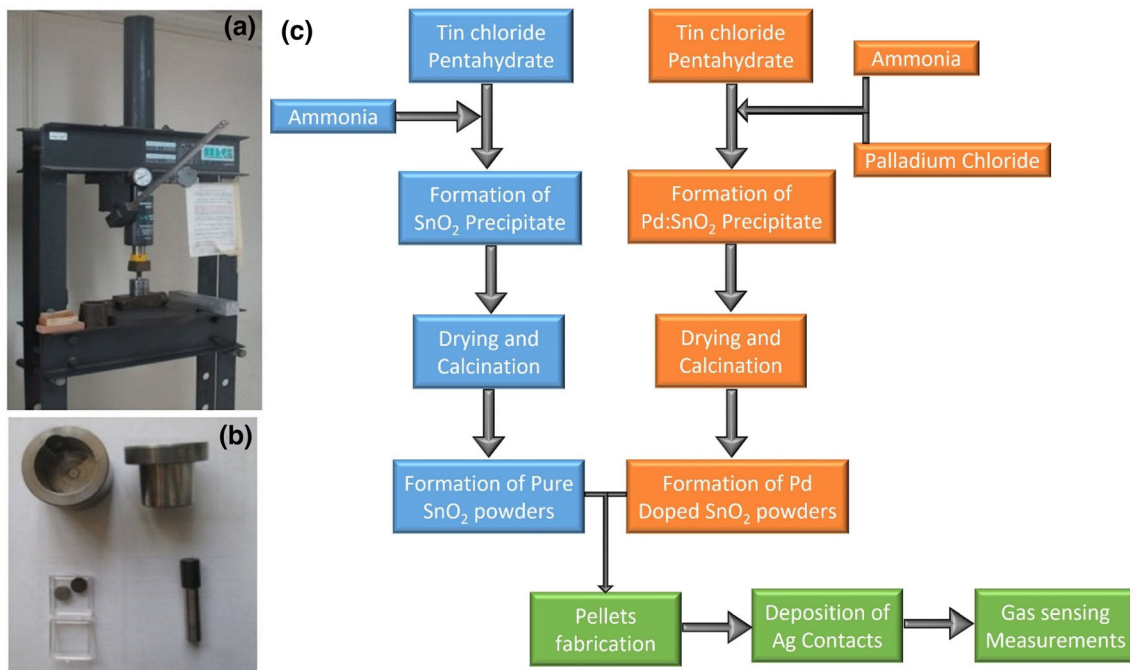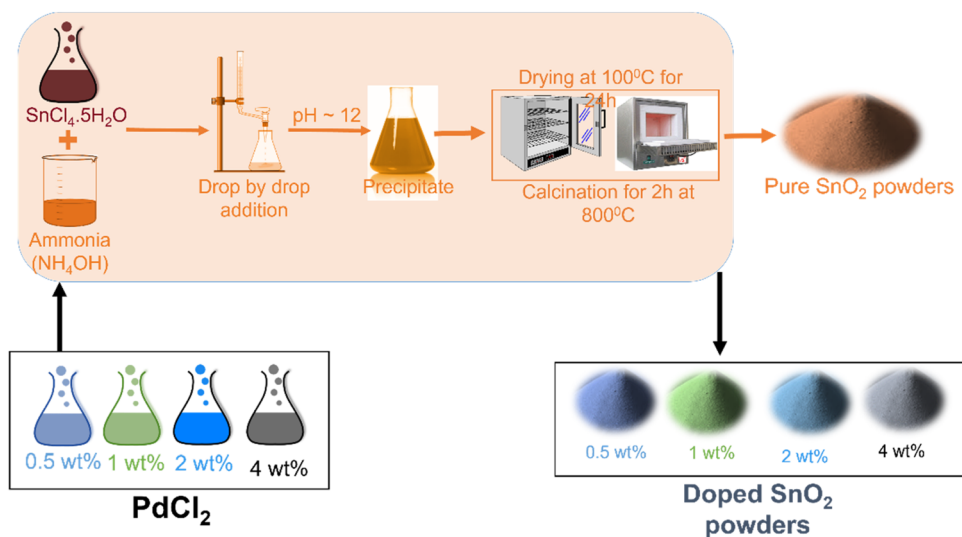Fig. 1 Wet chemical synthesis procedure of pure and doped SnO_2 powders

Fig. 2 IMR-pressing machine utilized in the pellet fabrication (a) and the dye components utilized (b)

nitrogen). A schematic diagram of the gas-sensing system was reported in our previous work [36].

3 Results and discussion

3.1 Structural properties

The undoped SnO_2 pellets were labeled as "Pure SnO_2" and palladium-doped SnO_2 pellets were labeled as "0.5 wt% Pd:SnO_2," "1 wt% Pd:SnO_2," "2 wt% Pd:SnO_2," and "4 wt% Pd:SnO_2," respectively, according to the Pd dopant wt% concentration. Figure 3a shows the X-ray diffraction spectra of the undoped and Pd-doped SnO_2 pellets. All the measured peaks exhibit the pure tetragonal rutile phase of SnO_2, according to the JCPDS Card 77-0450 [37] with a (110) as preferential orientation. Other SnO_2 crystal orientations observed are (101), (200), (111), (211), (220), (002), (310), (112), (301), (202), (212), and (321).
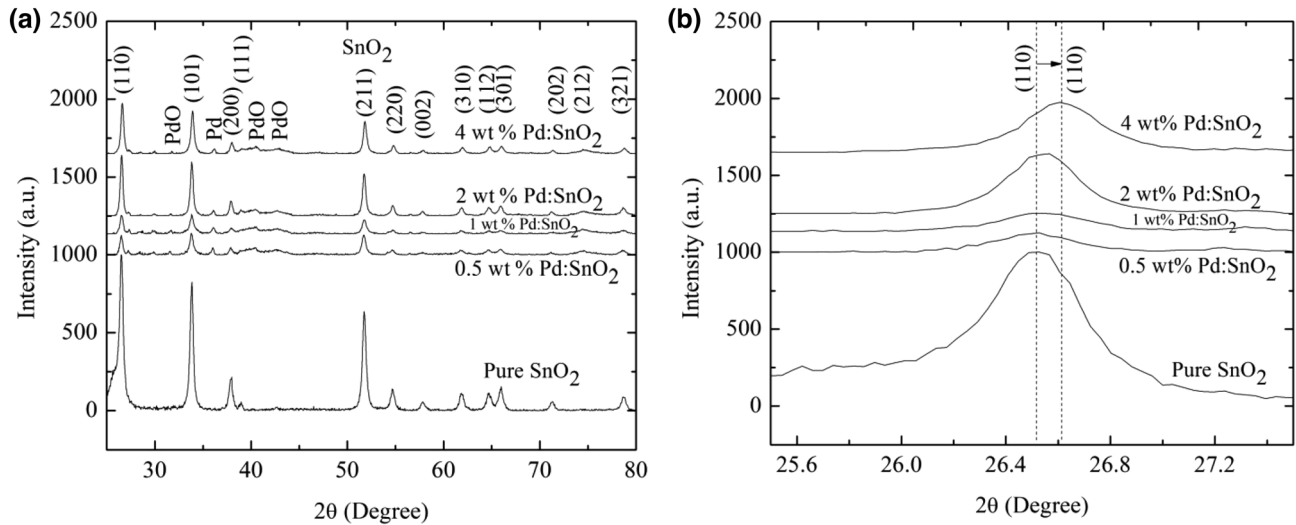
Fig. 3 a XRD diffractograms of pure and Pd-doped SnO_2 powders and **b** right shift in the (110) preferential orientation due to dopant incorporation

Also, from Fig. 3a, it is possible to observe that the diffraction peaks of metallic Pd and PdO confirms that some part of the dopant stayed in the metallic and oxidized cluster form on the surface of SnO_2, for all the doped samples. Authors believe that these clusters could be located in the intergranular zones. However, a right shift in the preferential orientation (110) diffraction peak was observed in the detailed analysis of preferential orientation, as shown in Fig. 3b. Increase in the Pd doping concentration resulted in higher angle shift of (110) peak, which may be due to the incorporation of the Pd into the SnO_2 crystal Lattice. Also, from Fig. 3a it is observed an uplift in the spectra of doped samples and this uplift increases with the increase in the amount of dopant concentration. This is also an indication of low crystallinity quality. A much-detailed analysis of the effect of dopant on crystalline quality is presented as follows.

The average crystallite size, D, and the lattice constants, c, and a of the SnO_2 powder were estimated from the X-ray spectra. D was obtained from the (110) peak, using the Scherrer's formula, Eq. (2) [38].

$$D = \frac{0.89\lambda}{\beta\cos\theta}, \qquad (2)$$

where the wavelength of X-ray, $\lambda = 1.5405$ Å, θ is the diffraction angle and β is the full width of the diffraction line measured at half of its maximum intensity, FWHM, the Gaussian function was used to

calculate the β full width of the diffraction line and the θ angle from diffraction patterns. The lattice constants, c and a can be estimated by using both (110) and (101) planes, (in the case of the tetragonal rutile phase, $a = b$) according to Eqs. (3) and (4) [39].

$$d_{hkl} = \frac{\lambda}{2\sin\theta_{hkl}}, \qquad (3)$$

$$\frac{1}{d_{hkl}} = \sqrt{\frac{h^2 + k^2}{a^2} + \frac{l^2}{c^2}}, \qquad (4)$$

where d_{hkl} is interplanar distances obtained from the Bragg law and along the crystal graphic directions (110) and (101), hkl is the diffraction angles of the (110) and (101) peaks. The texture coefficient $T_C(hkl)$ is the crystalline orientation of a particular plane, in this case,{hkl} is (110) plane, since this is the plane with the highest number of reflections with respect to the other crystalline planes. $T_C(hkl)$ is obtained from the measured intensity of peaks $I(hkl)$ and standard intensity peaks $I_S(hkl)$, and according with the equation [40].

$$T_C(hkl) = \frac{I(hkl)/I_s(hkl)}{n^{-1}\sum_n I(hkl)/I_s(hkl)}, \qquad (5)$$

where n is the number of peaks, $I(hkl)$ and $I_S(hkl)$ are the measured relative intensity of peaks to the (hkl) direction and standard intensity of peaks to the (hkl) direction taken from JCPDS database, respectively. If $T_C(hkl)$ values are higher than 1, there are a lot of planes oriented to the (hkl) direction, and if $T_C(hkl)$

values equal to or less than 1, therefore, most of the peaks show randomly oriented.

The values of the average crystallite size, D, lattice constants, c and a and texture coefficient, $T_C(hkl)$ of the pure and Pd-doped SnO_2 powders are shown in Table 1. From Table 1, it is observed that the average crystallite size remains close to 28 nm, regardless of the ratio Pd concentration. Increase in the ratio Pd wt% resulted in lower lattice constants, reaching its value in bulk, $a = b = 4.7382$ Å and $c = 3.187$ Å. These results suggest that the Pd atoms compress the basic cell of SnO_2, because their ionic radius is smaller than the ionic radii of Sn.

Regarding the texture coefficient, $T_C(110)$, it is observed that a lower concentration of Pd, the $T_C(110)$ drastically decreases and increases with Pd concentration, stating the growth of random orientation planes and undulations in the crystal lattice due to dopant incorporation. Finally, from the XRD analysis, it is clear that some part of the dopant was incorporated into the SnO_2 lattice which induced the structural changes and the remaining part stayed on the surface forming Pd and PdO clusters, which is evidenced in the upcoming HRTEM analysis section.

Also from the Williamson–Hall plot method, the crystallite size and microstrain were calculated, these were obtained from the values of peaks position 2θ, and the FWHM or β of all the observed diffraction peaks, and through the following equations:

$$\beta_{total} = \beta_{Sample} = \beta_{crystallitesize} + \beta_{microstrain}. \tag{6}$$

The Williamson method is used for non-zero residual stress, and this is based on the uniform stress deformation model, where β_{total} is the total peaks broadening or FWHM of the X-ray diffractogram, which contributes to the total peak broadening caused by the crystallite size, D (Eq. (2)) and by the total peaks broadening from the microstrain, ε, this is

Table 1 Average crystallite size, D, the lattice constants c and a, and texture coefficient $T_C(110)$

Film	D (nm)	a (Å)	c (Å)	$T_C(110)$
Pure SnO_2	~ 23	4.7515	3.1862	1.007
0.5 wt% Pd:SnO_2	~ 28	4.7565	3.1985	0.54
1 wt% Pd:SnO_2	~ 27	4.7464	3.1814	0.807
2 wt% Pd:SnO_2	~ 29	4.7439	3.1864	0.86
4 wt% Pd:SnO_2	~ 26	4.7357	3.1835	0.91

given by $\beta/4\tan\theta$. Therefore, the peak broadening total or total FWHM is given by Eq. (7).

$$\beta_{Total} = \frac{k\lambda}{D\cos\theta} + 4\varepsilon\tan\theta. \tag{7}$$

Substituting $\tan\theta = \sin\theta/\cos\theta$ and multiplying both sides by $\cos\theta$, we are left Eq. (7) as follows:

$$\beta_{Total}\cos\theta = \varepsilon(4\sin\theta) + \frac{k\lambda}{D}. \tag{8}$$

Equation (8) is a linear function, $y = mx + c$, where $y = \beta_{Total}\cos\theta$, slope, $m = \varepsilon$, $x = 4\sin\theta$ and the intercept, $c = \frac{k\lambda}{D}$. If we plot $4\sin\theta$ on the x-axis and $\cos\theta$ on the y-axis, the microstrain is the slope and crystallite size will be intercept, and the results are given in Table 2.

Scherrer's Eq. (2) gives a smaller crystal size D than that obtained from the Williamson–Hall method for non-zero residual stresses, Eqs. (6), (7) and (8). The stress leads to an increase in the peak width; therefore, using the Scherrer equation, the peak width or FWHM becomes too large which will give a smaller crystal size.

It is important to mention that XRD analysis confirms that doping with Pd increased the crystallite size, which may be due to either the growth of the crystal at planes with more undulations arise due to the incorporation of Pd into SnO_2 lattice or oxide formation of Pd. However, authors believe that the crystalline quality of the material has been decreased due to Pd incorporations. In order to confirm the crystalline quality, Raman analysis was performed.

3.2 Raman analysis

In order to study the effect of incorporation of dopant on the crystal quality and vibrational modes, Raman analysis was performed and the spectrum obtained is shown in Fig. 4. According to the results, the Raman spectra of SnO_2 nanopowders were best fitted to rutile, tetragonal tin oxide. Surface bands as well as bulk bands were observed. Results shown here are in good agreement with those reported by Nicolas Sergent, Mauro Epifani, Elisabetta Comini, Guido Faglia, and Thierry Pagnier (Interactions of nanocrystalline tin oxide powder with NO_2: A Raman spectroscopic study [41]).

The Raman bands of SnO_2 were detected at 472, 638, and 774 cm^{-1} corresponding to the three characteristic fundamental vibrational modes, namely, E_g,

Table 2 Average crystallite size, D and microstrain, ε by Williamson–Hall plot method

Film	Crystallite size, D (nm)	Microstrain, ε ($\times 10^{-3}$)
Pure SnO$_2$	~ 21	~ 0.8
0.5 wt% Pd:SnO$_2$	~ 45	~ 2.82
1 wt% Pd:SnO$_2$	~ 28	~ 1.76
2 wt% Pd:SnO$_2$	~ 34	~ 1
4 wt% Pd:SnO$_2$	~ 37	~ 1.7
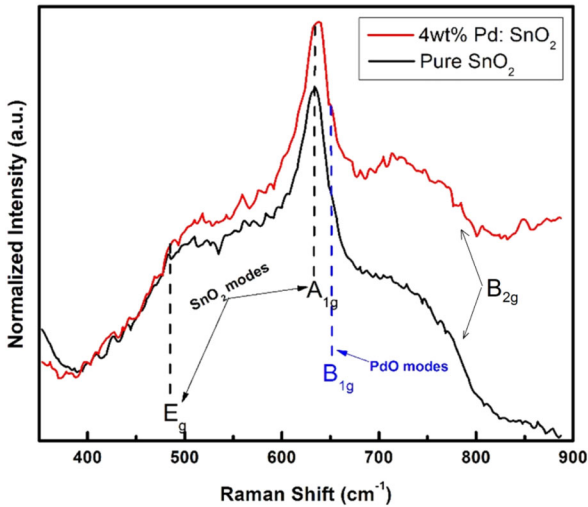
Fig. 4 Raman spectra of pure and 4 wt% Pd-doped SnO$_2$ powders

Fig. 5 The analysis of crystallinity calculation of SnO$_2$ powders by Raman spectrum

A_{1g} and B_{2g}, respectively. E_g mode has been identified as two oxygen atoms vibrating parallel to the c-axis, but in opposite direction. The peaks fitting at 638 cm^{-1} and 774 cm^{-1} of pure SnO$_2$ Raman spectrum can be assigned to the asymmetric stretching of Sn–O bonds of A1g and B2g, respectively. These vibrational modes found in our samples guarantee the tetragonal structure of SnO$_2$ nanoparticles reported in this work.

The shift towards right or higher wavelength confirming the possible substitution of Sn^{2+} ion with Pd^{2+} [42]. Additionally, for Pd-doped sample, a B1g tetragonal phase PdO mode was also observed [43], which was also confirmed by XRD analysis.

Finally, the relative crystallinity of the samples can be obtained according to the following formula [44].

$$X_C = \frac{V_B}{V_A + V_B}, \tag{9}$$

wherein X_C is the relative crystallinity, V_B is the crystalline region area, and V_A is the amorphous area, according to the following example, Fig. 5.

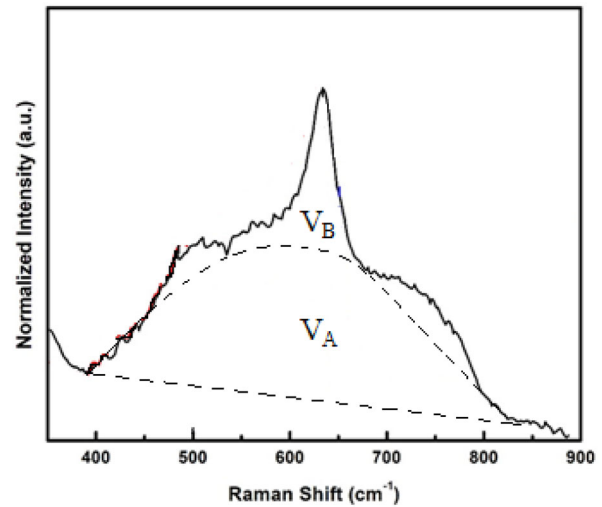All the results are shown in Table 3. Although the incorporation of the impurity element into the crystal lattice creates defects or disorders that result in the reduction of the symmetry of the lattice space [45]. It can be seen that the ratio between the crystalline area and the amorphous area is higher for the doped samples.

3.3 Morphological properties for pure and doped SnO$_2$ powders

Figure 6a–e shows the SEM images of Pure SnO$_2$, 0.5 wt% Pd:SnO$_2$, 1 wt% Pd:SnO$_2$, 2 wt% Pd:SnO$_2$, and 4 wt% Pd:SnO$_2$ samples, respectively. In general, more morphological changes were observed in both pure and Pd-doped powders. The surface morphology observed of all SnO$_2$ powders consisting of both nanometric particles and large grains, with a broad grain size distribution. The nanometric particles with an average particle size ranging between 20 and 40 nm in diameter. While the larger grains with irregularly shaped showing different crystalline planes, the average grain size was ranging from 200 to 500 nm. Both grain sizes have shown irregular shape, this may be due to the deposit technique in

Table 3 The relative crystallinity of two samples by Raman spectra

Sample	Relative total area, $V_A + V_B$ (a.u.)	Relative peak area, V_B (a.u.)	Relative crystallinity, X_C (%)
Pure SnO$_2$	121,093	23,950	19.77
4 wt% Pd:SnO$_2$	90,416	20,724	22.92
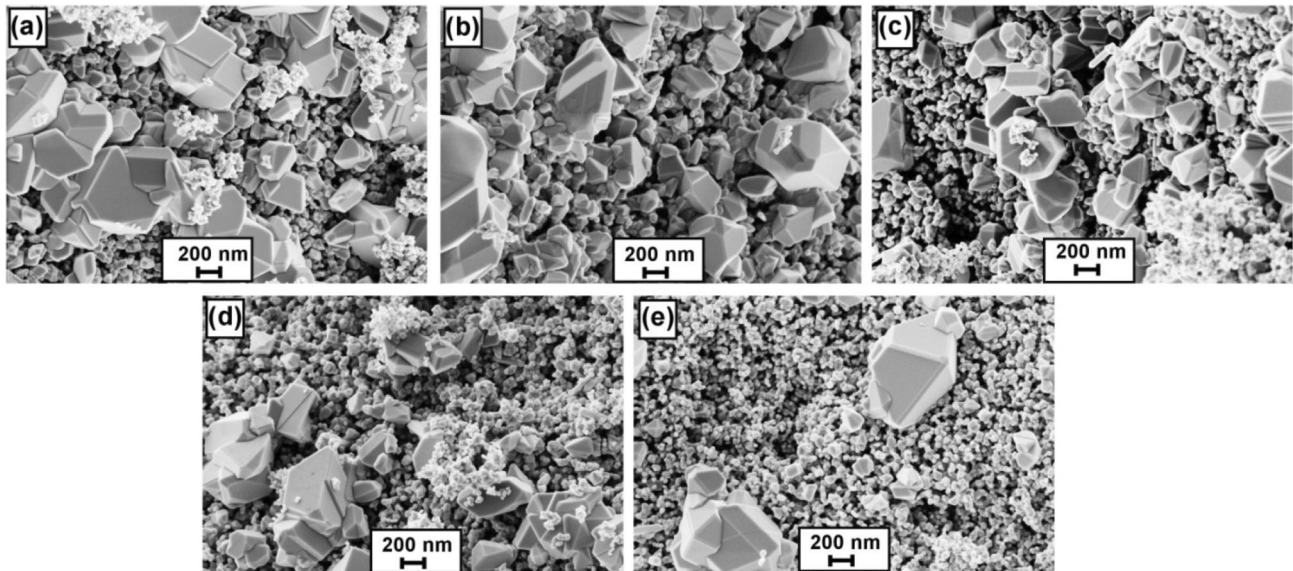
Fig. 6 SEM micrographs of **a** pure SnO$_2$, Pd doped with concentrations, **b** 0.5, **c** 1, **d** 2 and **e** 4 wt%

which the grinding and compression of powders intervene. The crystalline planes that present the largest grains are oriented towards the preferential crystallographic directions shown by the XRD measurements, these preferential crystallographic directions are [110], [101], [211]. It is evident from the SEM images that the increase in doping concentration reduced the number of larger grains with irregular morphology and increased the nanometric particles. Therefore, the 4 wt% Pd:SnO$_2$ sample possesses relatively more homogenous surface with uniform nanometric particle size, Fig. 6e. We believe that this may be due to the higher segregation of Pd at the grain boundaries, occupying interstitial places, preventing the grain from growing, and therefore, decreasing the number of larger grains [46]. Hence, it can be concluded that the Pd concentration has a great effect on the reduction of Pd-doped SnO$_2$ grain size.

Figures 7 and 8a–e show the SEM images of all obtained pure and Pd-doped tin oxide powders at higher magnifications. From Fig. 7a–e, it can be observed that all the images show grains with an

irregular shape. In general, we observed that as the amount of Pd dopant increases in the samples, the grain size decreases, for the reasons mentioned above. In the similar manner, it can also be noticed in the images that as the dopant concentration increases, the grain size decreases and also the SnO$_2$ particles become more homogeneous. For the pure SnO$_2$ samples, Fig. 7a, we can see grains of an average size of 10 to 30 nm and larger grain sizes ranging up to 300 nm, for the sample doped with 0.5 wt%, Fig. 7b, we can also observe grain with sizes above the 10 nm and large grains whose size increases up to 300 nm. For the sample doped with 1 wt%, Fig. 7c, the grain size ranges from 70 to 250 nm, for a sample doped with 2 wt%, Fig. 7d, the grain size ranges from 40 to 150 nm and for the samples doped with 4 wt%, Fig. 7e, the grain size It ranges from 50 to 150 nm, and the surface is less porous because it has a greater number of grains whose sizes are around 80 nm, that is, the surface/volume ratio is larger in comparison to other samples. It is observed that for samples doped with 1, 2, and 4 wt%, the grain size is more homogeneous as the amount of doping is increase.
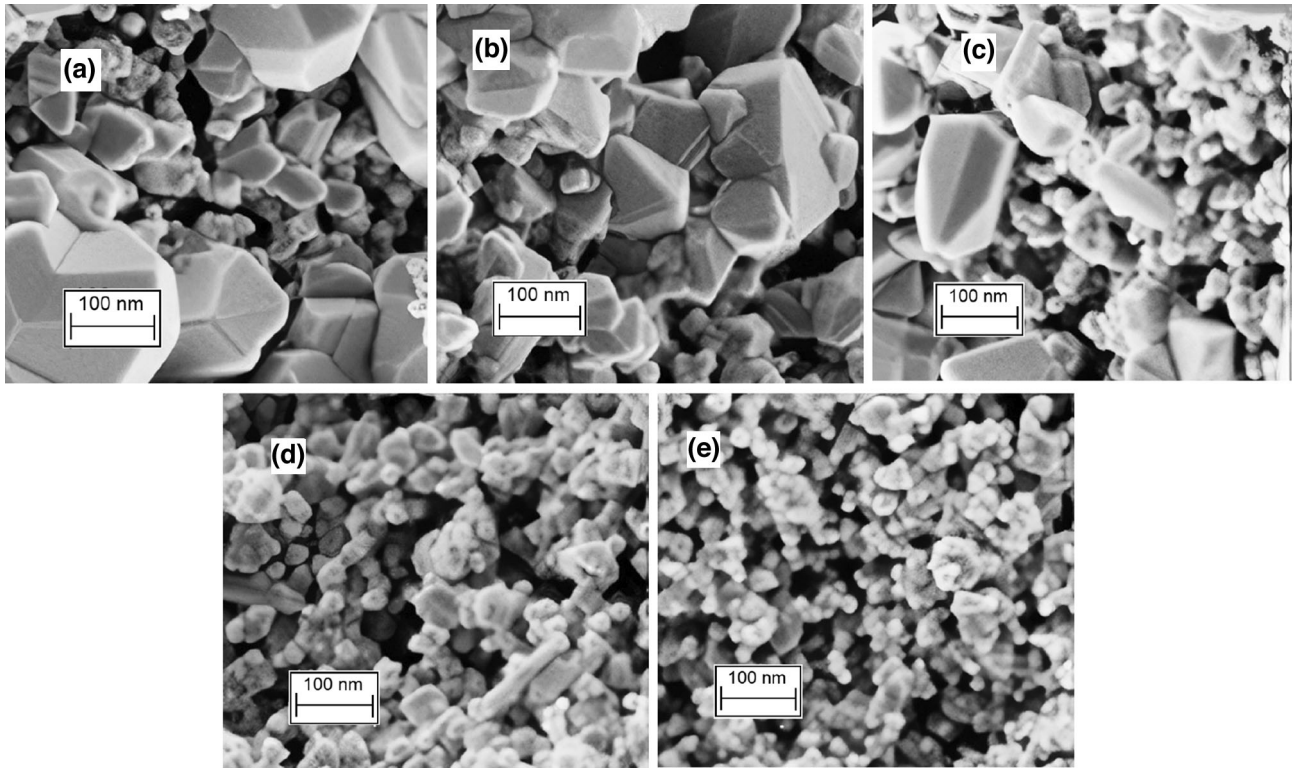
Fig. 7 100 nm magnification of SEM micrographs of **a** pure SnO_2, Pd doped with concentrations, **b** 0.5, **c** 1, **d** 2, and **e** 4 wt%

However, larger grains seem to grow by the coalescence of smaller grains.

For much smaller scales Fig. 8a–e, we can confirm from what has been said above, for pure and doped samples with 0.5 wt% of Pd, Fig. 8a, b, the morphological surfaces are made up of large, irregular grains showing crystalline planes and small irregular grains, for samples doped from 1 wt%, Fig. 8c–e, the surfaces change to irregular grains tending in some cases almost spherical and being less porous, that is, the number of large grains is disappearing and the number of small grains is increased.

3.4 Energy-dispersive spectroscopy (EDS) measurements

From energy dispersive spectroscopy elemental analysis, Fig. 9a–e, it was possible to verify the composition of the elements of pure and doped SnO_2 powders. The analysis was carried out in areas with higher density of material, such as in large grains or areas of high density of grains. Table 4 shows the atomic ratio Pd/Sn. It was observed that as the atomic percentage of palladium in the powder increases, the atomic ratio Pd/Sn is increased, and it

is verified that the atomic percentage of the palladium was close to the expected value.

3.5 High-resolution transmission electron microscopy (HRTEM) analysis

For obtaining more detailed morphological and structural details, TEM analysis of all powders was performed. It is important to mention that prior to TEM analysis, all powders were submitted to ultrasonication in ethanol for 30 min. Figure 10a–e shows the TEM images of pure SnO_2, 0.5 wt% Pd:SnO_2, 1 wt% Pd:SnO_2, 2 wt% Pd:SnO_2, and 4 wt% Pd:SnO_2, respectively. From the figures, it is evident that the formation of tetragonal-shaped particles with both larger grains and nanometric-sized particles. Besides a 30 min ultrasonication, still a large amount of agglomeration of the particles is observed for pure SnO_2 particles. The agglomeration and the number of large grains decrease with increase in the Pd dopant concentration. The nanometric size tetragonal particles possess a mean size ~ 20–30 nm.

In order to locate the dopant position, HRTEM analysis was performed and is shown in Fig. 11. Surface of pure SnO_2 is shown in Fig. 11a and its
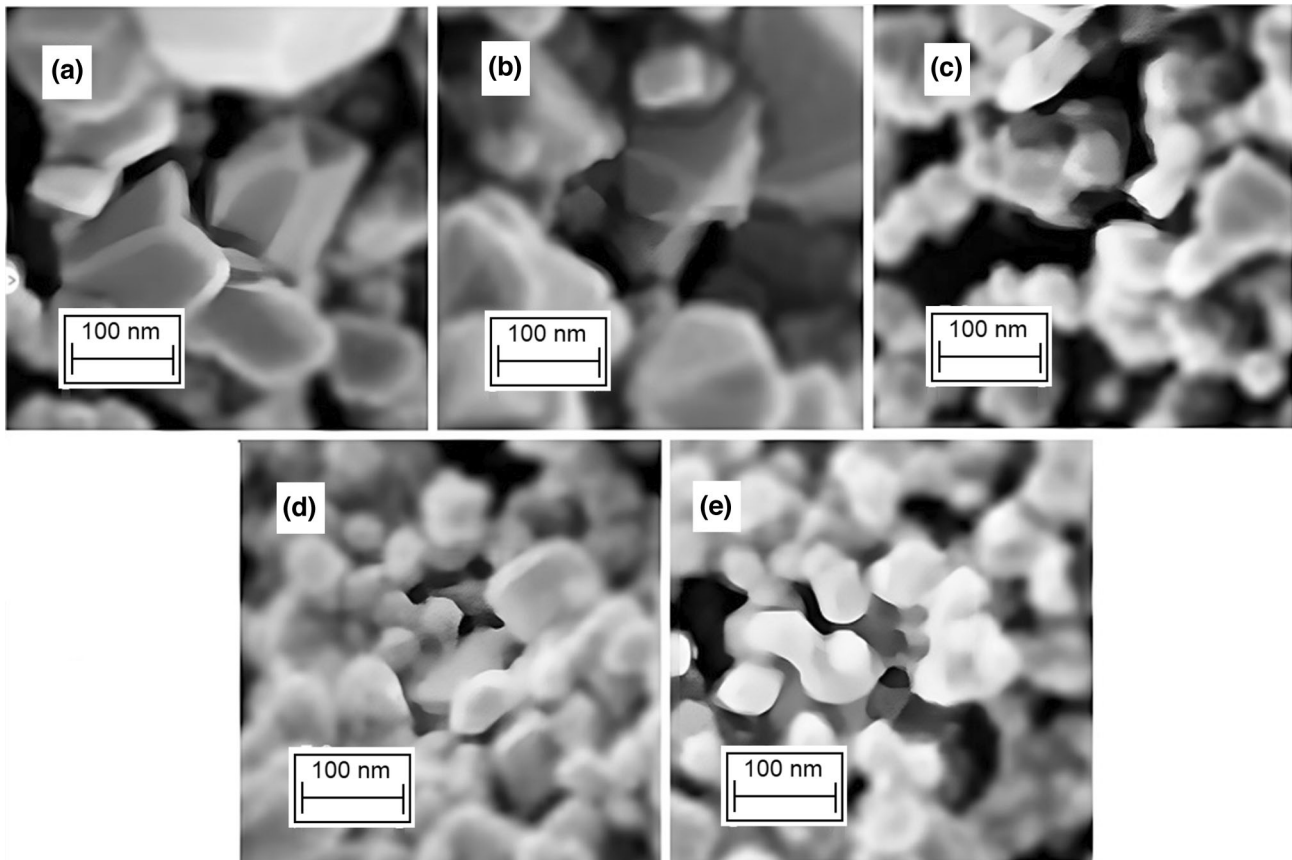
Fig. 8 50 nm magnification of SEM micrographs of **a** pure SnO$_2$, Pd doped with concentrations, **b** 0.5, **c** 1, **d** 2, and **e** 4 wt%

reconstructed FFT image is shown in Fig. 11c, it is observed that the lattice spacing corresponds to (110) plane of SnO$_2$ crystal lattice and the undulations observed in the reconstructed image are Moire patterns which arise due to the crystal overlap [47]. On the other hand, it is possible to see the rough surface with much smaller particles on the Pd-doped SnO$_2$ surface, see Fig. 11c. In the reconstructed image of Fig. 11c, it is possible to observe the difference in the crystal distance of the surface atom and the base SnO$_2$ structure. The lattice spacing of the smaller particles corresponds to metallic Pd, with size around 2 to 3 nm. Therefore, it is evident from TEM analysis that, a part of the dopant stayed at the surface in form of metallic clusters, which is favorable for gas-sensing applications. Also, from Fig. 11c and 10d, it can be observed that the interplanar distance of (110) plane of SnO$_2$ increased from 0.32 to 0.36 nm stating the incorporation of Pd into the crystal lattice, which is also the preferential orientation obtained from XRD analysis.

Additionally, it can be observed the SAED patterns of the pure and 4 wt%-doped SnO$_2$ samples from Figs. 10f and 11e. SAED patterns are in good agreement with the preferential orientation observed in the XRD. The four visible rings in both the SAED patterns correspond to (110), (101), (200), and (211) planes of SnO$_2$. These are the four planes with the highest relative intensity observed for all the samples in the XRD diffraction patterns. Also, additional traces of Pd or PdO were observed in SAED pattern of 4 wt% Pd-doped SnO$_2$ sample. This confirms the presence of dopant clusters on the surface of the SnO$_2$. Similar crystallite size, preferential orientation, morphology, and interplanar distances were reported by Yan et al. [48], where the authors obtained Pd-doped SnO$_2$ powders by solvothermal method with a particle size ranging between 20 to 30 nm from HRTEM analysis. However, authors did not vary the doping concentration and the obtained powders were utilized for VOC sensing.
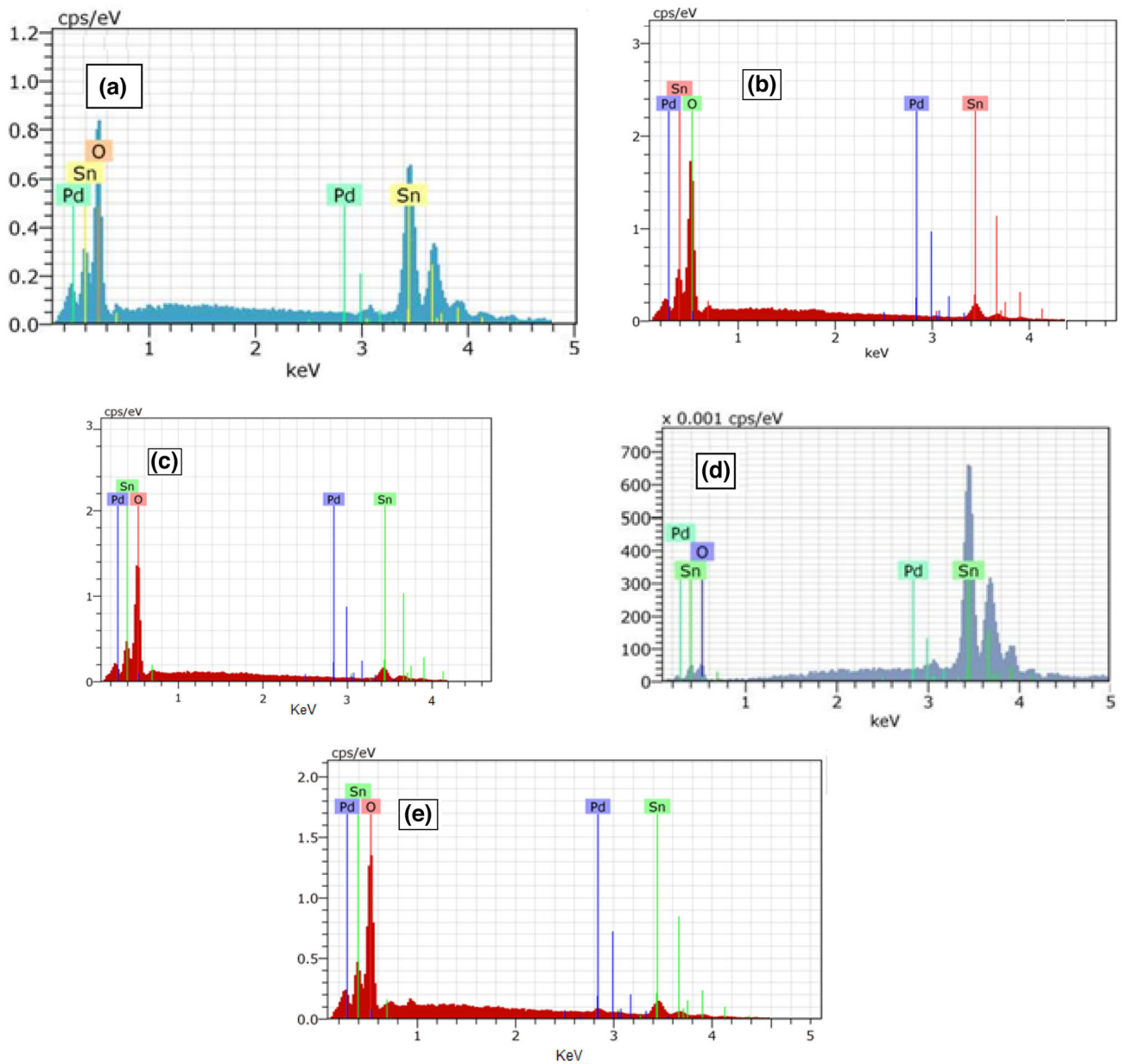
Fig. 9 EDS patterns of **a** pure SnO_2, Pd doped with concentrations, **b** 0.5, **c** 1, **d** 2, and **e** 4 wt%

Table 4 Pd/Sn atomic ratio values obtained from the EDS results

Sample	Pd/Sn ($\times$ 100%)
Pure SnO_2	0
0.5 wt% Pd:SnO_2	0.61
1 wt% Pd:SnO_2	1.2
2 wt% Pd:SnO_2	1.8
4 wt% Pd:SnO_2	5

3.6 Sensing properties

3.6.1 Sensing response

The sensing performance of both pure and Pd-doped SnO_2 pellets, as a function of the C_3H_8 concentration and operating temperature is presented and compared in Fig. 12a–e. It is observed that the sensing response increases with respect to both the operating temperature and propane gas concentration. This is
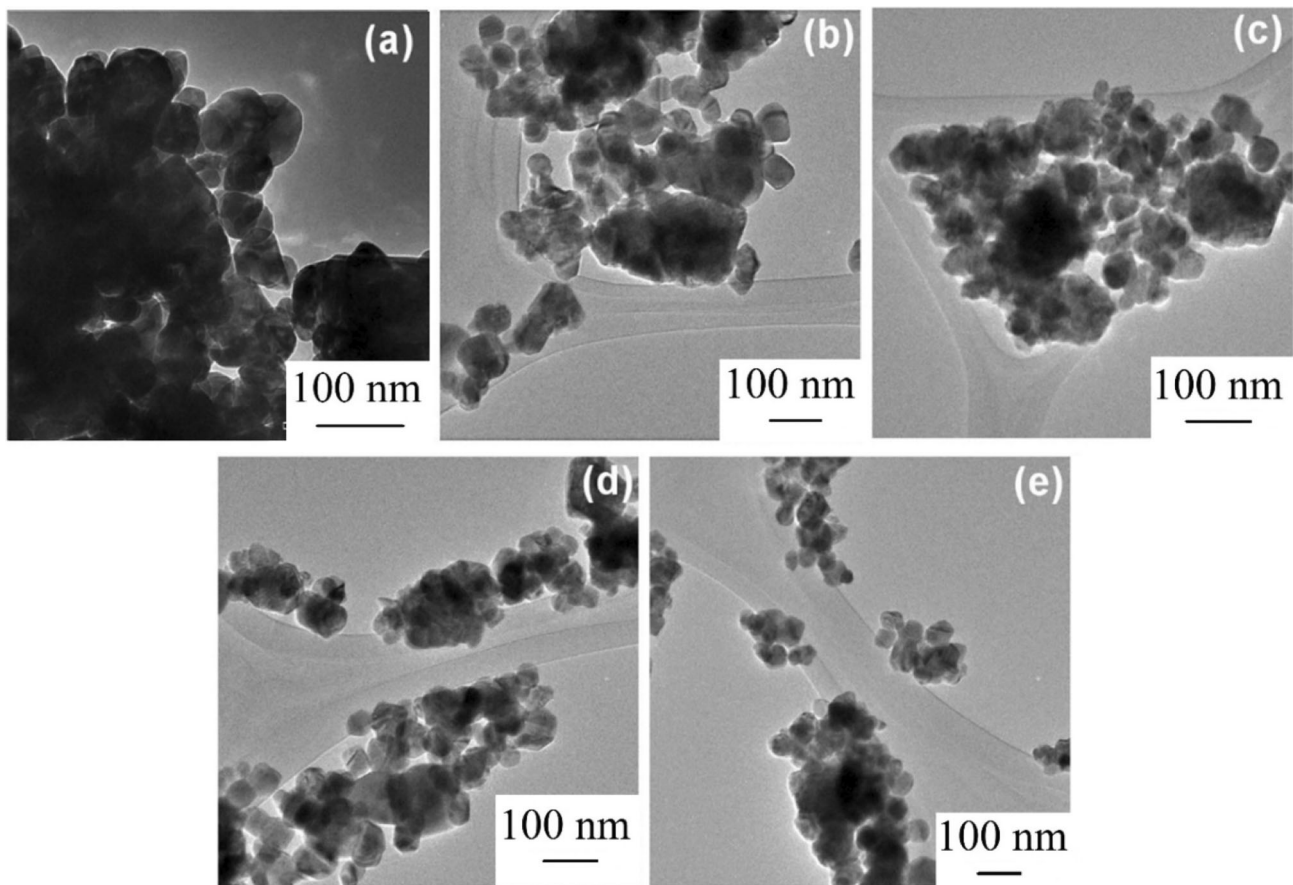
Fig. 10 TEM micrographs of SnO$_2$ powder doped by **a** 0, **b** 0.5, **c** 1, **d** 2, and **e** 4 of Pd wt% in the starting solution

very common phenomena that, the increase in operation temperature makes the oxygen molecule more reactive to react with test gas molecules and in case of higher gas concentrations makes the surface to react with more propane molecules resulting in higher responses [49]. The greatest increase in the sensing response occurs in the operating temperature range from 0 to 100 °C, above 100 °C the sensing response begins to saturate, which is an indication that the oxygen molecules on the surface of the SnO$_2$ are depleted.

Also, the sensing response for Pd-doped SnO$_2$ enhanced as compared to undoped SnO$_2$, and the increment is proportional to the Pd doping wt%, Fig. 12b–e. Authors believe that the Pd atoms on the surface act as a catalyst and increase the adsorption of oxygen. Also, it is confirmed by XRD, EDS, and Raman analysis that a part of dopant is incorporated into the SnO$_2$ crystal-generating defects, these defects also promote the electronic-sensing mechanism [50]. Maximum gas-sensing response was obtained for Pd-

doped SnO$_2$ powders with 4 wt% and was obtained at 300 ppm of C$_3$H$_8$, and measured at 300 °C as is shown in Fig. 12f. The increase in sensing response for 2 wt% and 4 wt% Pd-doped SnO$_2$ powders is not substantial. This can be attributed to the fact that Pd atoms saturate the SnO$_2$ surface forming agglomerates and oxides as observed in XRD and Raman analysis and preventing more adsorption of oxygen. As previously indicated for concentrations from 2 wt% of Pd in SnO$_2$, a large part of Pd is located in interstitial sites and intergranular zones, and therefore, has little effect on morphological and sensing properties.

It is necessary to clarify the importance of making sensing measurements with other gases such as CO and CO$_2$, to verify the selectivity that the samples have against other gases; however, it would remain as future work.

Additionally, the increase in higher sensing responses of doped samples is attributed to the porous and homogenous morphology observed in SEM

Fig. 11 HRTEM images of
a pure SnO_2, **b** 4 wt%
Pd:SnO_2, **c** reconstructed
HRTEM after masking of **a**,
d reconstructed HRTEM
image after masking of (**b**),
SAED patterns of **e** pure SnO_2
and **f** 4 wt% Pd:SnO_2
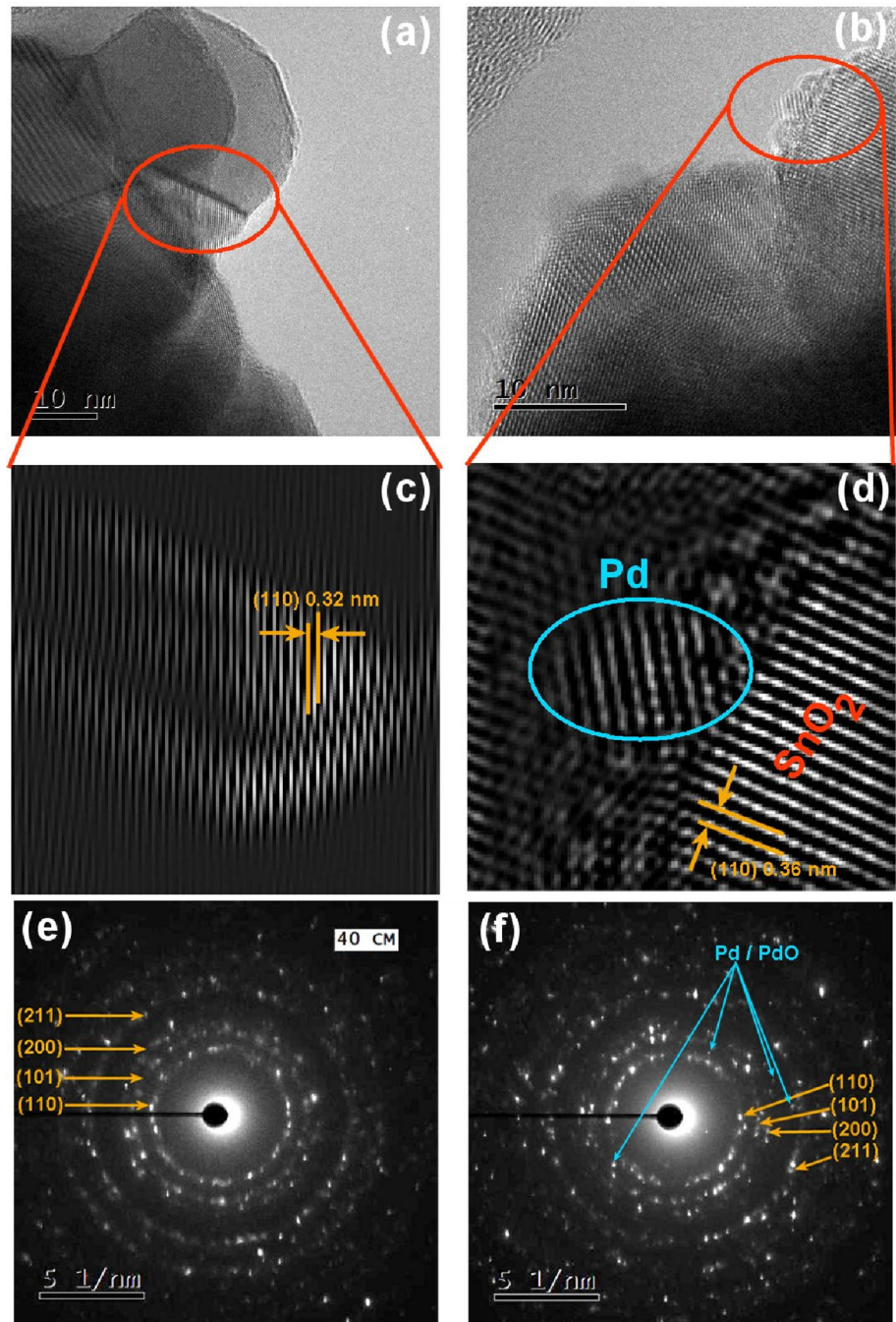
analysis. From Figs. 6, 7, and 8, it is evident that increase in dopant concentration reduced the particle size and resulted in uniform nanometric morphology. This increases the surface-to-volume ratio of the doped samples making the surface with more available adsorption sites, which subsequently increased the sensing response. Section 3.6.2 discusses the gas-sensing mechanism of pure and Pd-doped SnO_2 structures.

3.6.2 Sensing mechanism

The whole sensing process is ruled by the amount of adsorbed oxygen on the metal semiconductor surface $O_{2(abs)}$, because the target gas molecules react with
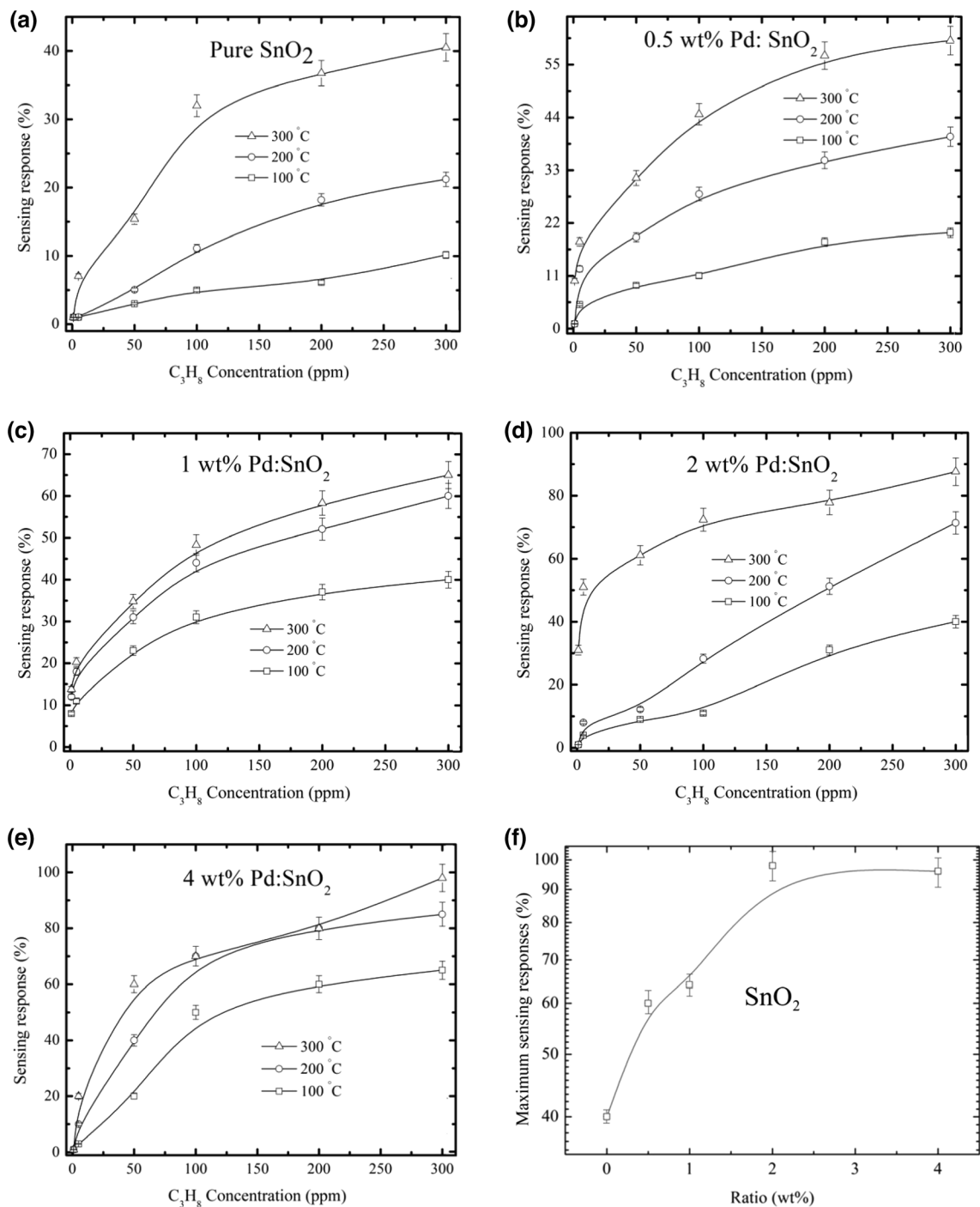
Fig. 12 Propane gas-sensing properties of **a** pure, **b** 0.5, **c** 1, **d** 2, **e** 4 wt% Pd-doped SnO_2 powders and **f** maximum sensing responses for SnO_2 powders doped with different percentages of Pd content
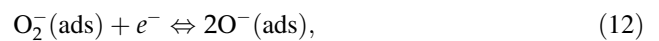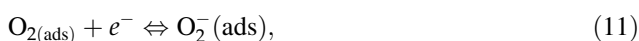
adsorbed surface oxygen to alter the surface electrical conductivity of the metal semiconductor, which is used as sensor signal. By varying the amount of absorbed oxygen, the number of dangling bonds on the surface and subsequently the number of free electrons vary. The amount of adsorbed surface oxygen varies with the operating temperature, at low operating temperatures [51, 52], below 150 °C,

Fig. 13 Energy band representation of the surface processes associated with the reaction in air (left) and C_3H_8 gas (right) for surfaces made up of undoped grains (**a**, **b**) and doped grains (**c**) and (**d**) with similar size. O^-, O^{2-} oxygen ion, single and double ionized, respectively, O_2^- molecular oxygen ionized, l is the thickness of charge depletion region, E_f, Fermi level energy, E_C, conduction band energy, E_C, valence band energy and ϕ_b, built-in potential
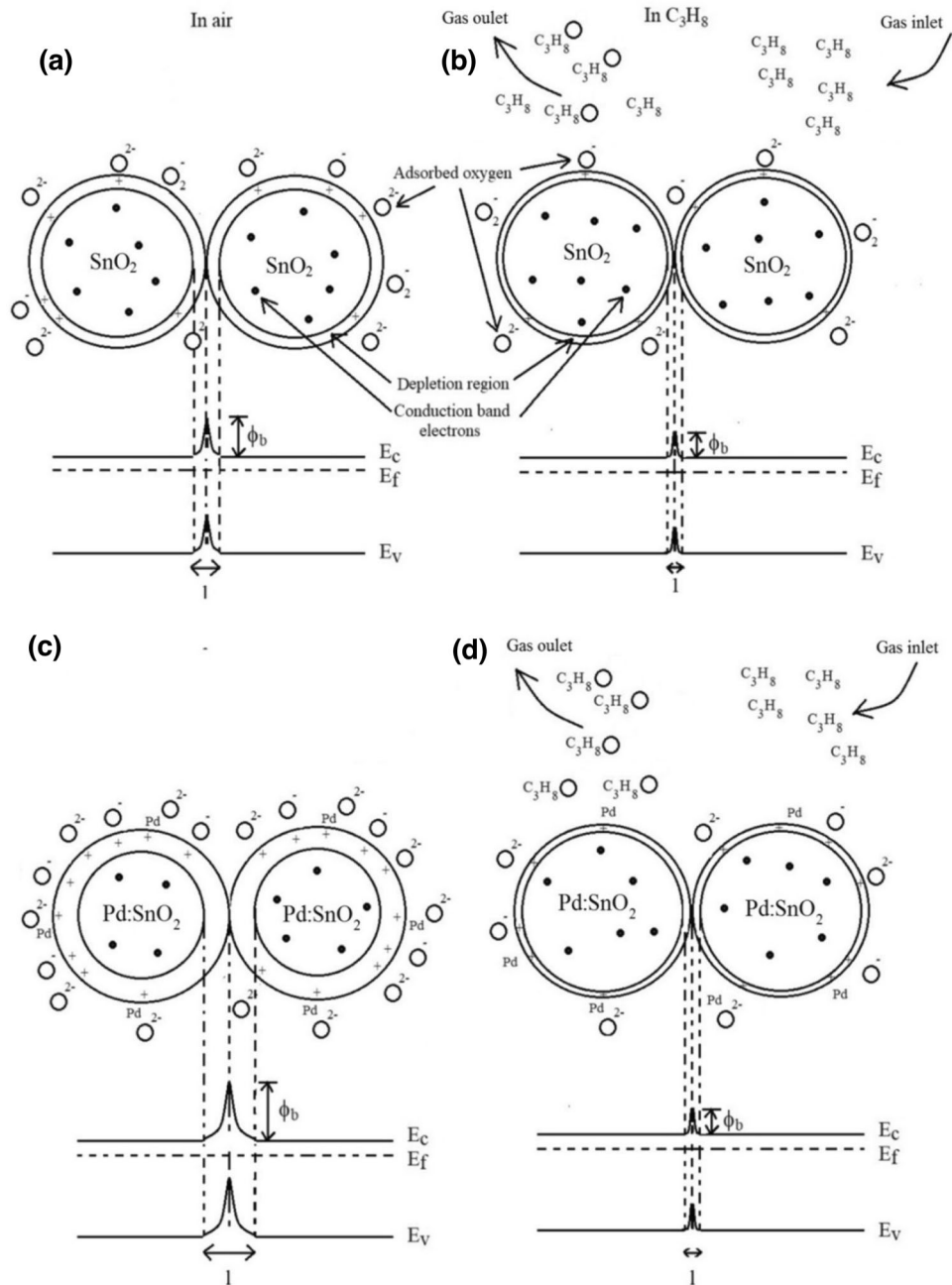
adsorbed oxygen appears in the form of oxygen molecular ion O_2^-, which would change to oxygen ion O^-, 150–400 °C temperatures and O^{2-} for temperatures above 400 °C as operating temperatures rising. The chemical adsorption process can be represented by the following reactions:

$$O_2(gas) \Leftrightarrow O_2(ads), \tag{10}$$

$$O_{2(ads)} + e^- \Leftrightarrow O_2^-(ads), \tag{11}$$

$$O_2^-(ads) + e^- \Leftrightarrow 2O^-(ads), \tag{12}$$

$$O^-(ads) \Leftrightarrow O^{2-}(ads). \tag{13}$$

The oxygen adsorption directly alters the thickness of the depletion region formed and, therefore, the surface built-in potential, ϕ_b [53] (Fig. 12a), and these factors determine the change in the surface electrical conductance, Eq. (1). Furthermore, the amount of absorbed oxygen is generally altered by the operation temperature since it provides the thermal energy to

produce more adsorption–desorption reactions on the surface. The presence of a catalyst such as Pd on the surface of SnO_2 favors more amount of adsorbed oxygen, which in turn increases the surface-free electrons capture, leaving a greater desertion region and a higher surface built-in potential, ϕ_b (Fig. 12c). The absorbed oxygen on the surface is desorbed when reacts with a reducing gas, such as C_3H_8, Fig. 12b. The more absorbed oxygen on the surface as is the case of doped SnO_2, the more the probability of desorbing oxygen from the surface which results a change in the surface electrical conductance, making the sensor response higher [54]. In Fig. 12d, it can be observed that the Pd ions on the surface enhance the sensor response (Fig. 13).

4 Conclusion

In this work, synthetized SnO_2 powders doped with Pd were obtained successfully by wet chemical synthesis. XRD results confirm the tetragonal rutile phase in SnO_2 and that a part of dopant was incorporated and the remaining stayed at surface in the form of clusters, and crystallite size increased from 23 to 28 nm with Pd doping. HRTEM analysis coincides with the XRD analysis confirming that the preferential orientation of all samples is (110) and the crystallite size ranges between 20 and 30 nm. A right shift in the preferential orientation suggests a particle incorporation of dopant into the SnO_2 crystal lattice, which may be due to the incorporation of the Pd into the SnO_2 crystal Lattice. Also the SAED patterns and DFT patterns confirm the presence of Pd cluster at surface and undulations in the SnO_2 lattice. Raman analysis confirms that the presence of peaks at 638 cm^{-1} and 774 cm^{-1} of pure SnO_2 Raman spectrum can be assigned to the asymmetric stretching of Sn–O bonds of A1g and B2g, respectively, and an increase in the crystalline quality due to Pd incorporation, although all the SnO_2 vibrational modes decrease for doped samples and its ratio of crystalline area to amorphous area is increased. Both irregular large grains around 200 nm and homogeneous particles around 20 nm were observed for pure SnO_2 sample in SEM analysis. Increase in dopant concentration decreased the number of larger grains and the particle size reduced from 300 to 30 nm. It was observed that as the dopant concentration increases, the grain size decreases. The smallest grain size $\sim$

40 nm and uniform morphology were observed when the Pd dopant concentration was 4 wt%, three magnification of SEM micrographs are presented to verify what has been said. In addition to HRTEM, EDS analysis also confirms the incorporation of Pd doping of each sample. Propane sensing responses were obtained for all the samples and 4 wt%-doped SnO_2 pellets exhibited a sensing response of near to 97% when measured at 300 °C. Pure SnO_2 sample exhibited a sensing response of 40%. The increase in the sensing response is attributed to the decrement in the particle size and catalytic effect on the surface of the nanograins. As confirmed by the structural and morphological analysis, the incorporation of doping into the SnO_2 lattice resulted in electronic-sensing mechanism and the surface Pd/PdO clusters provoked the spillover effects. Finally, we can conclude that by a simple and cost-effective method, the obtained chemical sensors based on SnO_2 can lead to a fabrication of devices with high response. Other parameters, such as dynamic characteristics, selectivity, and stability parameters will be considered in our future work in order to utilize the sensors in practical applications.

Author contributions

HG performed writing, TVKK and AGH interpretation of results and MLO and AM review and editing.

Data availability

I declare that all data used in this work are available. The datasets generated and/or analyzed during the current study are not publicly available due [have not

been published] but will be available from the data repository when the main manuscript will be published.

Declarations

Competing interests   Heberto Gomez Pozos, corresponding author of the work entitled "Propane gas sensing properties of pure and Pd doped tin oxide nanostructures" declare that there are no conflicts of interest on behalf of all the authors. The authors inform that no exist interests that are directly or indirectly related to the work submitted for publication within the last 3 years of beginning the work.

Ethical approval   There is no financial relationship with other people or organizations that could inappropriately influence this research work. I informed you that neither human nor animals were involved in this research.

References

1. T. Ikeda, K. Sato, Y. Hayashi, Y. Wakayama, K. Adachi, H. Nishimura, Sol. Energy Mater Sol Cells **34**, 379 (1994). https://doi.org/10.1557/PROC-1101-KK02-01

2. T. Waitz, B. Beckera, T. Wagnera, T. Sauerwald, C.D. Kohlb, M. Tiemann, Sensor Actuators B Chem. **150**, 788 (2010). https://doi.org/10.1016/j.snb.2010.08.001

3. D. Mohanta, K. Barman, S.J.M. Ahmaruzzaman, J. Colloid Interfaces Sci. **505**, 756 (2017). https://doi.org/10.1016/j.jcis.2017.06.064

4. P. Ravikumar, K. Ravichandran, B. Sakthivel, J. Mater. Sci. Technol. **28**, 999 (2012). https://doi.org/10.1016/S1005-0302(12)60164-9

5. Q. Wang, X. Li, W.-M. Zhao, S. Jin, Appl. Surf. Sci. **492**, 374 (2019). https://doi.org/10.1016/j.apsusc.2019.06.168

6. R.V. Vijayalakshmi, R. Kuppan, P.P. Kumar, J. Mol. Liq. **307**, 112951 (2020). https://doi.org/10.1016/j.molliq.2020.112951

7. M.W. Holdgate, *A Perspective of Environmental Pollution* (Cambridge University Press, New York, 1979). https://doi.org/10.1177/004711788000600518

8. M. Tucker, Ecol. Econ. **15**(3), 215 (1995). https://doi.org/10.1016/0921-8009(95)00045-3

9. C.A. McLinden, V. Fioletov, M.W. Shephard, N. Krotkov, C. Li, R.V. Martin, M.D. Moran, J. Joiner, Nat. Geosci. **9**, 496 (2016). https://doi.org/10.1038/ngeo2724

10. J.L. Peel, R. Haeuber, V. Garcia, A.G. Russell, L. Neas, Biogeochemistry **114**, 121 (2013). https://doi.org/10.1007/s10533-012-9782-4

11. H. Sugie, C. Sasaki, C. Hashimoto, H. Takeshita, T. Nagai, S. Nakamura, M. Furukawa, T. Nishikawa, K. Kurihara, Forensic Sci. Int. **143**, 211 (2004). https://doi.org/10.1016/j.forsciint.2004.02.038

12. J.M. Bautista, A. Maldonado, M.L. Olvera, Gas sensing performance of TiO_2–Al_2O_3 pellets, in *2015 12th International Conference on Electrical Engineering, Computing Science and Automatic Control (CCE)* (2015). https://doi.org/10.1109/ICEEE.2015.7357971

13. H.G. Bonilla, M.F. Martínez, V.M.R. Betancourtt, A.G. Bonilla, J.R. Gómez, L.G. Ortiz, M.L. Olvera, J.S. Salazar, Sensors **16**, 177 (2016). https://doi.org/10.3390/s16020177

14. R.S. Aashis, A.R. Koppalkar, M. Sasikala, T. Machappa, P.M.V.N. Ambika, Sens. Lett. **9**, 1342 (2011). https://doi.org/10.1166/sl.2011.1679

15. A. Maldonado, S.A. Mallen-Hernandez, J. Vega-Perez, M.L. Olvera, Rev. Mex. Fis. **55**(1), 90 (2009)

16. C. Sankar, V. Ponnuswamy, M. Manickam, R. Mariappan, R. Suresh, Appl. Surf. Sci. **349**, 931 (2015). https://doi.org/10.1016/j.apsusc.2015.04.198

17. X. Zhao, B. Cai, Q. Tang, Y. Tong, Y. Liu, Sensors **14**, 13999 (2014). https://doi.org/10.3390/s140813999

18. W. Liu, X. Cao, Y. Zhu, L. Cao, Sensors Actuators B Chem. **66**, 219 (2000). https://doi.org/10.1016/S0925-4005(00)00347-6

19. J. Kaur, R. Kumar, M.C. Bhatnagar, Sensors Actuators B Chem. **126**, 478 (2007). https://doi.org/10.1016/j.snb.2007.03.033

20. D. Liting, L. Haiying, L. Shuo, L. Liu, L. Yu, X. Suyan, G. Yimin, C. Yali, Z. Xiangan, L. Qingcheng, Chem. Phys. Lett. **713**, 235 (2018). https://doi.org/10.1016/j.cplett.2018.10.052

21. A.I. Khudiar, A.M. Oufi, Sensor Actuators B Chem. **340**, 129633 (2021). https://doi.org/10.1016/j.snb.2021.129633

22. B. Gautheron, M. Labeau, G. Delabouglise, U. Schmatz, Sensor Actuators B Chem **16**, 357 (1993). https://doi.org/10.1016/0925-4005(93)85210-2

23. W. Zeng, T. Liua, D. Liu, E. Han, Sensors Actuators B **160**, 455 (2011). https://doi.org/10.1016/j.snb.2011.08.008

24. N.L. Moghadam, E.B.A. Karimabad, S.M. Niasari, H. Safardoust, J. Nanomater. **5**, 47 (2015)

25. M.I. Amer, S.H. Moustafa, M. El-Hagary, Mater. Chem. Phys. **248**, 122892 (2020). https://doi.org/10.1016/j.matchemphys.2020.122892

26. A.D. Bhagwat, S.S. Sawant, B.G. Ankamwar, C.M. Mahajan, J. Nano Electron. Phys. **7**, 04037 (2015)

27. L.A. Patil, M.D. Shinde, A.R. Bari, V.V. Deo, Sensors Actuators B Chem. **143**, 270 (2009). https://doi.org/10.1016/j.snb.2009.09.048

28. R. Herrera-Rivera, M.L. Olvera, A. Maldonado, J. Nanomater. **1**, 9 (2017). https://doi.org/10.1155/2017/4595384

29. D. Soumen, V. Jayaraman, Prog. Mater. Sci. **66**, 112 (2014). https://doi.org/10.1016/j.pmatsci.2014.06.003

30. S. Sagadevan, J. Podder, Soft Nanosci. Lett. **5**, 64 (2015). https://doi.org/10.4236/snl.2015.54007

31. E.M. El-Maghraby, A. Qurashi, T. Yamazaki, Ceram. Int. **39**, 8475 (2013). https://doi.org/10.1016/j.ceramint.2013.01.112

32. I.M.E. Radaf, T.A. Hameed, G.M.E. Komy, T.M. Dahy, Ceram. Int. **45**, 3072 (2019). https://doi.org/10.1016/j.ceramint.2018.10.189

33. J.K. Srivastava, P. Pandey, V.N. Mishra, R. Dwivedi, Solid State Sci. **11**, 1602 (2009). https://doi.org/10.1016/j.solidstatesciences.2009.06.014

34. J.K. Srivastava, D.K. Verma, R.M.L. Awadh, Int. J. Sci. Res. Dev. **9**, 2321 (2021)

35. A.R. Phani, Appl. Phys. Lett. **71**, 2358 (1997). https://doi.org/10.1063/1.120557

36. K.K. Tangirala-Venkata, M.L. Olvera, A. Maldonado, R.R. Biswal, H. Gómez-Pozos, Sensors **20**(23), 6879 (2020). https://doi.org/10.3390/s20236879

37. J. Haines, J.M. Léger, Phys. Rev. B. **55**, 11144 (1997). https://doi.org/10.1103/PhysRevB.55.11144

38. B.D. Cullity, S.R. Stock, *Elements of X-ray Diffraction*, 3rd edn (Prentice Hall, Upper Saddle River, 2001)

39. F.T. Leitão Muniz, M.A. Ribeiro Miranda, C.M. dos Santos, J.M. Sasaki, The Scherrer equation and the dynamical theory of X-ray diffraction. Acta Crystallogr. A **72**, 1–6 (2016). https://doi.org/10.1107/S205327331600365X

40. G.B. Harris, Quantitative measurement of preferred orientation rolled uranium bars. Philos. Mag. **43**, 113–123 (1952). https://doi.org/10.1080/14786440108520972

41. N. Sergent, M. Epifani, E. Comini, G. Faglia, T. Pagnier, Sensor Actuators B Chem. **126**, 1 (2007). https://doi.org/10.1016/j.snb.2006.10.013

42. M.I. Ivanovskaya, P.A. Bogdanov, D.R. Orlik, ACh. Gurlo, V.V. Romanovskaya, Thin Solid Films **296**(1–2), 41–43 (1997). https://doi.org/10.1016/S0040-6090(96)09354-6

43. A. Ayeshamariam, S. Ramalingam, M. Bououdina, M. Jayachandran, Spectrochim. Acta Part A Mol. Biomol. Spectrosc. **118**, 1135–1143 (2014). https://doi.org/10.1016/j.saa.2013.09

44. Y. Liu, Y. Xu, Y. Yan, D. Hu, L. Yang, R. Shen, Starch/Stärke **67**, 612–619 (2015). https://doi.org/10.1002/star.201400246

45. H.F. Franzen, *Second-Order Phase Transitions and the Irreducible Representation of Space Groups*. Lecture Notes in Chemistry, vol. 32 (Springer, Berlin, Heidelberg, 1982). https://doi.org/10.1007/978-3-642-48947-1_1

46. H. Gómez-Pozos, A. Maldonado, M.L. Olvera, Mater. Lett. **61**, 1460 (2007). https://doi.org/10.1016/j.matlet.2006.07.053

47. G. Oster, Y. Nishijima, Moiré patterns. Sci. Am. **208**, 54 (1963)

48. W. Yan, X. Zeng, G. Wu, W. Jiang, D. Wei, M. Ling, H. Zhou, C. Guo, J. Mater. Sci. Mater. Electron. **31**, 14165 (2020). https://doi.org/10.1007/s10854-020-03971-x

49. M.J. Madou, S.R. Morrison, *Chemical Sensing with Solid State Devices* (Academic Press, London, 1989)

50. X. Zhou, A. Wang, Y. Wang, L. Bian, Z. Yang, Y. Bian, Y. Gong, X. Wu, N. Han, Y. Chen, ACS Sensors **3**(11), 2385 (2018). https://doi.org/10.1021/acssensors.8b00792

51. M. Che, A.J. Tench, Adv. Catal. **31**, 77–133 (1982)

52. S.C.J. Chang, Vac. Sci. Technol. **17**, 366–369 (1980). https://doi.org/10.1116/1.570389

53. M.W.J. Prins, K.-O. Grosse-Holz, J.F.M. Cillessen, L.F. Feiner, J. Appl. Phys. **83**(2), 888–893 (1998). https://doi.org/10.1063/1.366773

54. Q.H. Wu, J. Li, S.G. Sun, Curr. Nanosci. **6**, 525–538 (2010). https://doi.org/10.2174/157341310797574934